Direct numerical simulations of round jets: Vortex induction and side jets

P. Brancher, J. M. Chomaz, and P. Huerre
LADHYX, Ecole Polytechnique, 91128 Palaiseau Cedex, France

(Received 21 April 1993; accepted 30 December 1993)

In this paper, a numerical investigation of three-dimensional round jets subjected to streamwise and azimuthal perturbations is reported. The main objective of the study is to give a consistent scenario for the breaking of rotational symmetry in such flows which may ultimately lead to the production of intense side jets. In particular it is shown that the development of the Widnall instability on the primary vortex rings and the evolution of the Bernal and Roshko [J. Fluid Mech. **170**, 499 (1986)] streamwise vortices generated by the instability of the braid could be deeply intertwined. A comprehensive discussion of the vortex induction mechanisms leading to the reorientation of the initial vorticity both in the ring and braid regions and to the deformation of the rings is presented. The recent analysis by Monkewitz and Pfizenmaier [Phys. Fluids A **3**, 1356 (1991)] is confirmed in the sense that strong radial ejection of fluid is not directly linked to the deformation of the vortex rings but rather to the occurrence of coherent streamwise vortex pairs. However, the final relative position of the streamwise vortex pairs with respect to the deformations of the vortex rings differs slightly from Monkewitz and Pfizenmaier's proposition.

I. INTRODUCTION

Recent experiments have shown that low-density round jets undergoing global oscillations[1–3] display a distinctly different spatial development from naturally evolving homogeneous jets. Such synchronized flows are subjected to a primary instability of the Kelvin–Helmholtz type resulting in the axisymmetric roll-up of the jet shear layer into highly regular vortex rings, which are phase locked to the global oscillations. Moreover, a new mode of entrainment is then observed in the near field of the jet: the radial ejection of fluid into secondary side jets normal to the main jet axis and distributed azimuthally in the form of quasiplanar sheets. Further experiments[1,2,4,5] have confirmed that the same phenomenon takes place in homogeneous jets strongly forced at Strouhal numbers of around 0.4. The synchronization of the primary vortex rings therefore seems to be the key feature for the generation of strong side-jets.

Different secondary instability mechanisms have been proposed as possible candidates for side-jet production. Monkewitz[1] first suggested that the Widnall[6] instability of the vortex rings themselves might be responsible. This azimuthal instability giving birth to lobes was expected to induce ejection of fluid away from the jet axis. But the recent numerical study of Martin and Meiburg[7] and quantitative measurements by Monkewitz and Pfizenmaier[5] and Liepmann and Gharib[8] have indicated that the side-jet phenomenon may bring into play pairs of streamwise vortices resulting from the instability of the region between the rings (the "braid"), which are the analog of the Bernal and Roshko[9] vortical structures in the plane shear layer.

One can find an interesting discussion on the secondary instabilities of a temporally developing mixing layer by Metcalfe *et al.*[10] Their direct numerical simulations confirmed the conjecture of Bernal and Roshko, namely the existence of three-dimensional instabilities in the form of counter-rotating streamwise vortices. These structures are responsible for the mushroom-shaped features observed in the experiments,[9] of which the side jets could be the amplified form. But to our knowledge, there have been few numerical studies focusing on the origin of these streamwise structures in the round jet case and their role in the side-jet phenomenon. So, in order to identify the respective influences of the secondary instabilities and to study the vortex induction mechanisms involved, we have numerically investigated the temporal evolution of a homogeneous round jet. The present direct numerical simulations are conducted in the same spirit as Martin and Meiburg's inviscid vortex filament computations.[7] They turn out to confirm some of their results while allowing to go further into the nonlinear regime and to take viscous effects into account.

II. NUMERICAL METHOD

The incompressible Navier–Stokes equations are integrated in a three-dimensional (3-D) periodic box using a pseudospectral code developed by Vincent and Meneguzzi.[11]

The vorticity form of the Navier–Stokes equations for incompressible flow is

$$\frac{\partial \mathbf{u}}{\partial t}=\mathbf{u}\times\omega-\frac{\nabla\Pi}{\rho}+\nu\nabla^2\mathbf{u}, \qquad (1)$$

$$\nabla\cdot\mathbf{u}=0, \qquad (2)$$

where $\mathbf{u}$ is the velocity, $\omega=\nabla\times\mathbf{u}$ the vorticity, ρ the density, $\Pi=p+\frac{1}{2}\rho(\mathbf{u}\cdot\mathbf{u})$ the pressure head, and ν the kinematic viscosity.

In Fourier space, Eqs. (1) and (2) can be reduced to

$$\frac{\partial \mathbf{u}_k}{\partial t}=\mathbf{P}(k)\cdot(\mathbf{u}\times\omega)_k-\nu k^2\mathbf{u}_k, \qquad (3)$$

where the tensor $\mathbf{P}$ is the projector on the space of solenoidal fields:

 1070-6631/94/6(5)/1768/7/$6.00

$$\mathbf{P}_{ij}(k)=\delta_{ij}-k_ik_j/k^2. \tag{4}$$

The right-hand side of Eq. (3) is computed by means of a pseudospectral method. A detailed review of the pseudospectral techniques is given for instance by Canuto *et al.*[12] The time stepping is done using a second-order finite-difference scheme. An Adams–Bashforth scheme is used for the nonlinear term while the dissipative term is integrated exactly.

The calculations were done with 64^3 Fourier components on a Cray-2. The collocation points are distant by $\delta x=2\pi/64$ and the time step is chosen to be equal to $\delta t=10^{-2}$ to fulfill the convergence conditions of the numerical scheme (the optimal time step given by the Courant criterion is observed to stay between 1.18×10^{-2} and 1.38×10^{-2} in all the simulations). The choice of viscosity, imposed by the spatial resolution, leads to a Reynolds number Re based on the jet radius of about 500. Care has been taken to avoid numerical artifacts. Thus, in order to suppress the artificial symmetries of the discrete grid, the jet axis was slightly shifted from the center of the box. The lateral periodic boundary conditions may also influence the dynamics. A radius equal to 1 for a box length L of 2π has been taken for which the effect of the periodicity was not noticeable. Indeed the natural evolution of the jet flow did not present spurious symmetries and an initial $n=3$ azimuthal symmetry imposed at $t=0$ persisted up to 30 turnover times as described later. Finally, no significant quantitative change in the flow development was observed during a test simulation with a 128^3 resolution (see Sec. III), thereby indicating that the 64^3 discretization was sufficient to bring out the main physical mechanisms involved in the side-jet phenomenon. Intensive three-dimensional visualizations of both velocity and vorticity fields were performed with the software EXPLORER on a Silicon Graphics workstation.

The basic flow is taken to be the axisymmetric velocity profile studied from a spatial point of view by Michalke:[13]

$$U(r)=0.5\{1+\tanh[0.5R/\theta(1-r)]\},$$

where the radial distance r and the streamwise velocity U are nondimensionalized with respect to the jet radius R and the axial jet velocity U_j. Consequently time t is nondimensionalized with respect to R/U_j. This velocity profile depends on the nondimensional parameter R/θ, where θ is the momentum thickness of the shear layer. A preliminary inviscid temporal linear stability analysis of this profile was performed numerically. A shooting method is used to integrate the linearized Rayleigh equation in cylindrical coordinates so as to generate the unstable linear eigenmodes pertaining to the basic flow $U(r)$. Each mode can be characterized by its azimuthal wave number m and its Strouhal number $\mathrm{St}=R/\lambda$, where λ denotes the streamwise wavelength. A standard test of numerical methods is the comparison between the growth rates predicted by linear stability theory and those obtained with the three-dimensional temporal calculations. Table I compares the growth rates σ_{LT} calculated from linear theory for different values of R/θ and St and σ_{NS} obtained from the direct simulations initialized with the corresponding unstable mode determined from linear theory. One can notice the good agreement between both sets of results with the relative error $\epsilon=(\sigma_{\mathrm{NS}}-\sigma_{\mathrm{LT}})/\sigma_{\mathrm{LT}}$ varying between 0.9% and 2.8%.

TABLE I. Growth rates of jet flow predicted by the linear stability analysis and obtained with the direct simulations.

St	R/θ	σ_{LT}	σ_{NS}	ϵ
0.40	11.3	0.042 29	0.0416	+0.0163
0.36	22.6	0.032 81	0.0325	+0.0094
0.81	22.6	0.046 41	0.0451	+0.0282

In the present paper, we focus on the particular basic flow at $R/\theta=11.3$. For this profile, the axisymmetric eigenmode $m=0$ corresponding to $\mathrm{St}=0.4$ happens to be the most unstable and it is therefore the one that appears naturally. In all the numerical simulations to be presented here, the basic velocity profile $R/\theta=11.3$ is initially perturbed by the most unstable axisymmetric eigenmode according to linear theory with an amplitude level equal to $|u_{\max}|/U_j\sim3\%$. In this way a regular development of the *primary* instability is induced which is similar to the synchronization observed experimentally in forced spatially developing jets.

The development of the *secondary* instabilities is triggered by adding to the previously defined initial conditions three different types of symmetry-breaking perturbations.

- In the first set of simulations referred to as the "NN" case, no additional secondary disturbances are imposed at $t=0$ and the jet is only subjected to the numerical noise produced by discrete grid effects and the influence of the periodic lateral boundary conditions. The most unstable eigenmode at $m=0$ then gives rise to a periodic array of rotationally symmetric vortex rings. The NN simulation is used as a reference case for the axisymmetric development of the primary instability.
- In the second set of simulations referred to as the "WN" case, white noise with an amplitude level equal to $|u'_{\max}|/U_j\sim5\%$ is added to the initial conditions to mimic the random fluctuations that are present in all experimental situations. A gradual breakdown of axisymmetry is then observed to occur "naturally."
- To control its evolution, a third kind of direct simulation denoted "AP" is carried out, whereby a well-defined azimuthal perturbation of the basic flow is introduced at $t=0$. More specifically a small radial displacement is initially applied to the inflection point of the basic velocity profile so that at time $t=0$, $U_0(r,\varphi)=U\{r[1+\epsilon\cos(n\varphi+\delta\varphi)]\}$, where φ is the azimuthal angle, $\delta\varphi$ a phase reference, and ϵ the amplitude of the deformation. Such a modulation produces the same effect as the corrugated nozzle used experimentally.[4] A similar scheme with $n=3$ has been used in the experiments of Monkewitz and Pfizenmaier[5] to stabilize the planes of the side jets at fixed azimuthal angles. In the same fashion, Martin and Meiburg[7] chose $n=5$ in their vortex filament computations. According to the analysis of Pierrehumbert

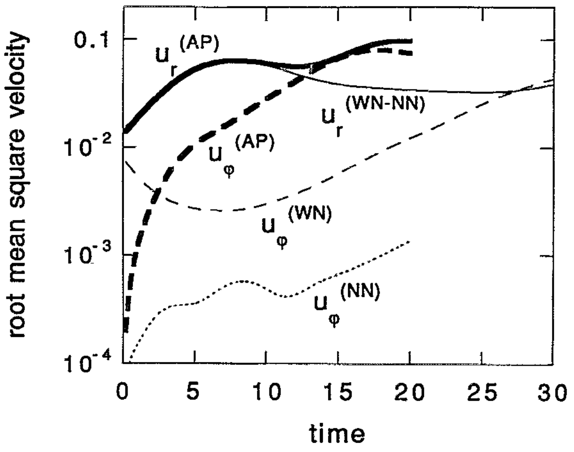

FIG. 1. Temporal evolution of the root mean square values of the radial (solid lines) and azimuthal (dashed lines) velocity for the WN (thin lines) and AP (thick lines) cases. For clarity, the NN radial velocity is not plotted but its evolution exactly coincides with the corresponding WN curve. The NN azimuthal velocity is represented by dotted lines.

and Widnall,[14,15] the primary Kelvin–Helmholtz vortices of plane shear layers are most unstable to secondary perturbations of the translative kind with a spanwise wavelength equal to two-thirds of the basic streamwise wavelength, a value which is in good agreement with the experimental observations of Bernal and Roshko.[9] If this result is extrapolated to the periodic array of vortex rings at St=0.4, one obtains $n=3$ as the most unstable secondary mode. This is fully consistent with the fact that the $n=3$ mode indeed appears "naturally" during the WN simulations. For this reason, the $n=3$ modulation was selected as input for the AP simulations.

III. RESULTS

Figure 1 presents the time evolution of the root mean square values of the radial and azimuthal velocity over the extent of the periodic box for the three classes of simulations:

$$u_r(t)=\sqrt{\frac{1}{L^3}\int\int\int u_r^2(x,y,z,t)dx\,dy\,dz},$$

$$u_\varphi(t)=\sqrt{\frac{1}{L^3}\int\int\int u_\varphi^2(x,y,z,t)dx\,dy\,dz},$$

where L is the size of the computational box; u_r and u_φ are, respectively, the contributions of the radial and azimuthal components to the total kinetic energy per volume unit in the computational box. In a concern for the clarity of the figure, the radial velocity in the NN case has not been represented because it is undistinguishable from the corresponding WN curve all along the NN simulation until $t=20$.

First we focus on the history of the radial velocity u_r, which is associated with the primary instability and the formation of the vortex rings. In all three simulations, the radial velocity grows linearly during the first time steps. Its initial growth rate is in adequate agreement with linear theory (Table I), which validates the numerical method. Saturation occurs around $t=6$, corresponding to the formation of coherent vortex rings. The slow decrease in the NN and WN simulations is due to viscous dissipation. In the NN case, the velocity field is observed from 3-D visualizations to stay nearly axisymmetric until the end of the simulation. The very weak departure from axisymmetry may be measured by the root mean square value of the azimuthal velocity u_φ, which is observed to stay two to three orders of magnitude below its radial counterpart, thus suggesting that the breaking of axisymmetry due to the periodicity of the lateral boundaries is negligible. By contrast, in the WN case the azimuthal velocity u_φ rapidly increases, beyond an early transient adjustment phase, and reaches around $t=25$ the same order of magnitude as the radial velocity u_r. In the AP simulation, the breakdown of axisymmetry is seen to be much more sudden and appears even before the saturation of the primary instability, thereby suggesting a loss of axisymmetry on the part of the rings themselves. During the last iterations of the WN simulation and above all at the end of the AP case, one can observe a renewed increase of the radial velocity, as the azimuthal velocity reaches comparable magnitudes. We will see that this excess of the radial velocity content over the WN case is no longer attributable to the rings but to the radial ejection of fluid away from the jet axis. The test simulation with the same conditions as the AP case but a 128^3 resolution was performed up to ten turnover times. The u_r and u_φ corresponding curves match with the AP ones within 0.074% and 0.55%, respectively, thereby allowing us to be confident in the results of the 64^3 simulations.

Figure 2 presents side views of the jet flows at time $t=25$ for the WN case [Fig. 2(a)] and at time $t=16$ for the AP case [Fig. 2(b)]. Isosurfaces of azimuthal (light gray) and streamwise (dark gray) vorticity are outlined. One can notice the similarity between these two figures which display the same qualitative features. In both, the azimuthal vorticity, associated with the primary vortex rings, is still coherent though strongly distorted azimuthally and longitudinally, as revealed by the presence of streamwise vorticity in the rings themselves. One can clearly observe receding outer lobes on the vortex rings, as in all experiments with side-jet production according to Raghu *et al.*[16] It must be emphasized that, in the case of Fig. 2(b), these lobes do not correspond to the initial corrugation of the basic flow but are π-out-of-phase with it, as explained later.

Another interesting feature is the presence of strong streamwise Bernal and Roshko[9] vortical structures, associated with dark isosurfaces of streamwise vorticity "knitting" between two consecutive vortex rings and aligned with the deformation of the rings. A detailed study of their signs indicates their gathering into pairs of counter-rotating round vortices. The cross sections in the braid region of the radial velocity field u_r in the WN [Fig. 3(a)] and AP [Fig. 3(b)] cases both display a nonaxisymmetric distribution of positive radial velocity (white areas). Similar sections at different streamwise locations present the same features suggesting that this radial velocity field cor-

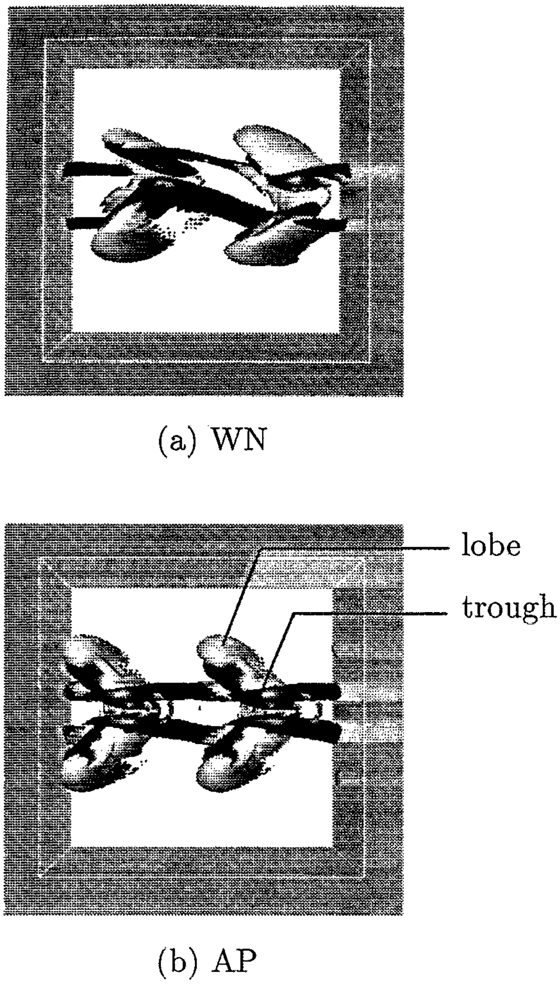

FIG. 2. Isosurfaces of the azimuthal (light gray) and streamwise (dark gray) vorticity at a threshold value corresponding to 40% of the respective maxima. For clarity, only the foreground is displayed: (a) WN simulation at $t=25$ ($\omega_\varphi=1.2$, $\omega_z=0.9$); (b) AP simulation at $t=16$ ($\omega_\varphi=1.9$, $\omega_z=1.6$).

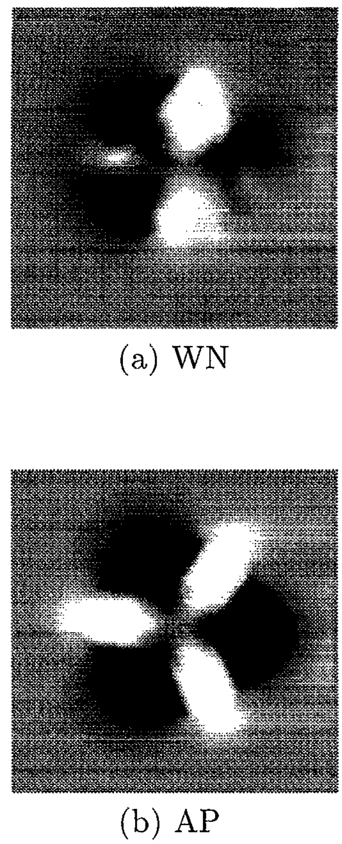

FIG. 3. Cross sections of the radial velocity field in the braid region. The gray scale ranges from less than -0.3 (black) to more than 0.3 (white): (a) WN case; (b) AP case.

responds to the ejection of fluid into coherent side jets. Comparison with the previous 3-D visualizations leads to the conclusion that the secondary jets are located in the troughs of the distorted rings, in good agreement with Liepmann and Gharib.[8] This configuration is consistent with the fact that streamwise vortices also lie in pairs within the troughs of the rings. They are of such a sign as to induce strong outward velocities in the troughs (white areas of Fig. 3) and weak inward velocities in the lobes (black areas of Fig. 3). Such a velocity field tends to fold back the receding outer lobes of the rings toward the jet axis and corresponds to the engulfing of external fluid between the side jets, as observed in previous experiments.[1,2] One should note the importance of mode 3 in the WN case, which is a justification for the choice of the AP initial conditions, as discussed previously. The exploitation of similar visualizations during the entire AP simulation allows us to propose the following scenario leading to side-jet generation.

Until $t=6$, the initial azimuthal vorticity of the basic flow concentrates into ring regions while the regions in between (braid regions) become depleted. As observed experimentally,[16] the whole azimuthal vorticity field occupies a cone-shaped zone with axis aligned with the flow and apex pointing downstream. At $t=6$, the primary instability has just saturated in the form of coherent vortex rings. The corresponding streamwise location would be $x/R=2$ to 3 if one relates streamwise distance to time via the real part of the phase velocity according to linear theory, assuming that the velocity profile at the jet nozzle is given by the basic flow with $R/\theta=11.3$.

While the primary instability grows, the initial corrugation imposed on the jet flow leads to the reorientation of vorticity both in the ring and braid regions. Figure 4(a) displays a cross section of the streamwise vorticity field in the braid region at the beginning of the simulation ($t=1$). One can observe an azimuthal distribution of streamwise vorticity which is synchronized with the initial corrugation in the form of weak sheets of alternatively positive (white) and negative (black) values. At a later time ($t=2$), the braid region on Fig. 4(b) presents the same distribution as Fig. 4(a) though more concentrated and amplified when compared with the initial azimuthal corrugation. By contrast, the streamwise vorticity in the ring region at $t=1$ [Fig. 4(c)] is distributed in quite the same way but it is π-out-of-phase with the corresponding configuration in the

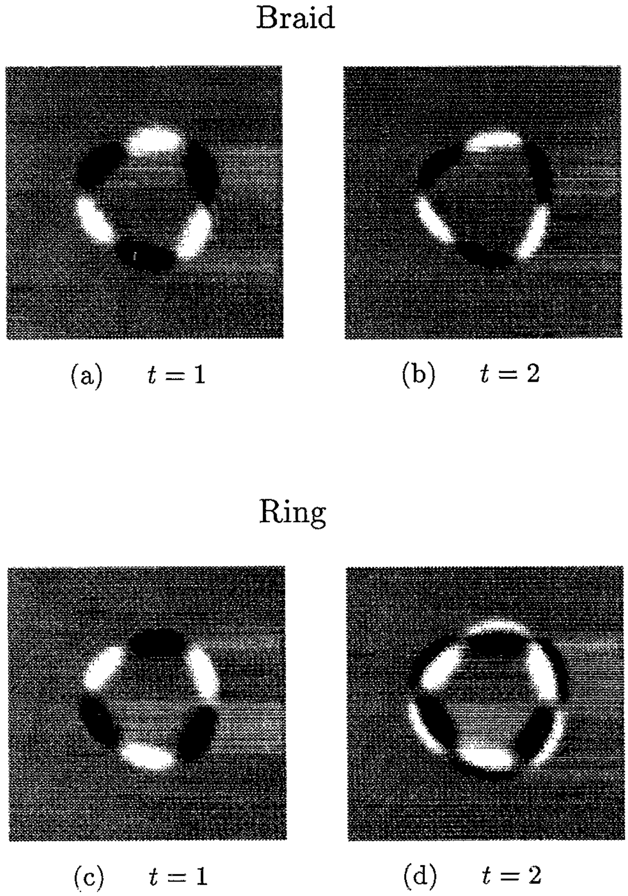

FIG. 4. Cross sections of the streamwise vorticity field; AP simulation; in the braid: (a) $t=1$, (b) $t=2$; in the ring: (c) $t=1$, (d) $t=2$. The gray scale ranges from -0.06 (black) to 0.06 (white) at $t=1$ (a), (c) and from -0.13 (black) to 0.13 (white) at $t=2$ (b), (d).

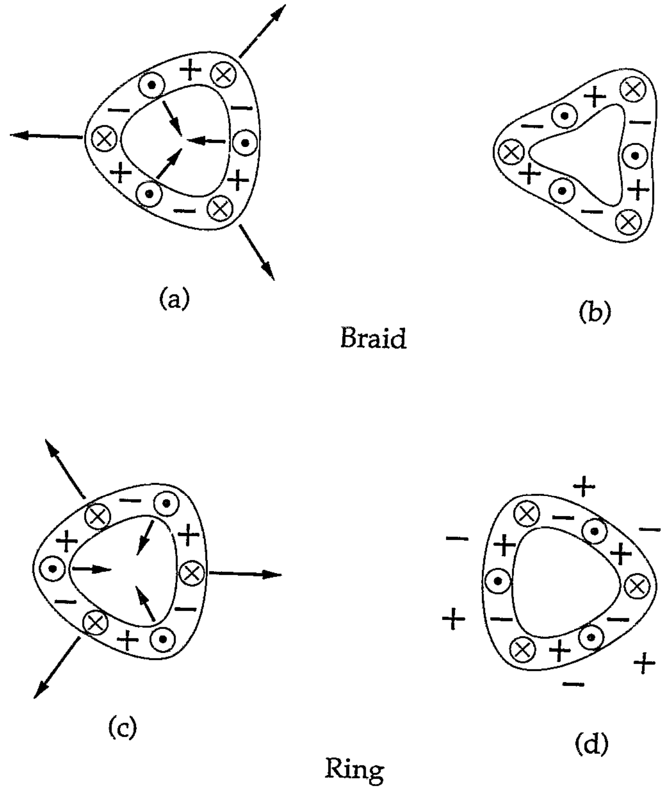

FIG. 5. Vortex induction mechanisms in the braid (a), (b) and ring (c), (d) regions. The relative motions are represented by arrows, circled crosses, and circled dots while + and − symbols refer to the sign of the local streamwise vorticity, the + sign corresponding to the vorticity directed downstream.

braids [Fig. 4(a)]. Thus, at the same azimuthal location, the sign of the streamwise vorticity is reversed between rings and braids. Finally, at $t=2$, an additional distribution of streamwise vorticity appears in the ring region [Fig. 4(d)] at the outer periphery of the previous one. A closer examination of 3-D visualizations reveals that this vorticity comes from the braid region located immediately downstream which begins to roll up around the ring.

In the following, we appeal to vortex induction arguments in order to account for the arrangement of the vortical structures. The sketches in Fig. 5 summarize the different induction mechanisms taking place both in the rings and in the braids. Each of the four diagrams provides an interpretation of the corresponding streamwise vorticity distributions displayed in Fig. 4. In the braid region [Fig. 5(a)], *global* induction by the array of vortex rings on the slightly corrugated azimuthal vorticity field tends to make the inner parts travel faster (circled dots) and the outer parts travel slower (circled crosses). This mechanism gives birth to an azimuthal distribution of streamwise vorticity with alternate sense of rotation indicated by the + and − signs in Fig. 5(a). Such a configuration is qualitatively similar to the computed results displayed in Fig. 4(a). In turn, the velocity field [arrows in Fig. 5(a)] induced by this newly created streamwise vorticity tends to increase the initial deformation as shown in Fig. 5(b) [to be compared with Fig. 4(b)].

A similar reasoning, based this time on *local* induction arguments, may be applied in the ring region, as indicated in Fig. 5(c). Because of their higher curvature, the outer lobes of the deformed vortex rings tend to travel faster (circled dots) while the inner troughs travel slower (circled crosses). The ensuing relative motion creates a distribution of streamwise vorticity of alternate + and − sign, which displays a π phase shift with respect to the corresponding distribution in the braid region of Fig. 5(a). Note the good qualitative agreement with the computed results of Fig. 4(c). In turn, the streamwise vorticity in the rings induces a radial motion indicated by the arrows in Fig. 5(c), which, at a later time, tends to turn the receding troughs into receding outer lobes and the advancing lobes into advancing troughs as shown in Fig. 5(d). This stage in the evolution is typical of elliptical vortex filaments as described for instance in Liu *et al.*[17] Finally the configuration of Fig. 5(d) is maintained in quasiequilibrium by the existence of an outer layer of streamwise vorticity issuing from the braid region located immediately downstream: the induction effect associated with this outer layer counteracts the velocities produced by the streamwise vorticity in the rings themselves. At this stage, the rings display receding outer lobes that are π-out-of-phase with the initial corrugation [compare Figs. 5(b) and 5(d)]. As in Martin and Meiburg,[7] we have noted, during this early phase of the simulation, that the streamwise vorticity in the braids is much more intense just downstream of the ring region than it is immediately upstream.

As the primary instability saturates, the initially weak sheets of streamwise vorticity in the braids resulting from the previous induction mechanisms are stretched by the increasing extensional strain field due to the vortex rings and they begin to roll to form streamwise vortices. This stretching mechanism is similar to the one described by Corcos and Lin[18] and Neu[19] in the case of plane shear layers. More specifically, these authors have demonstrated that an array of alternating weak vortices undergoing stretching in the axial direction collapses into pairs of counter-rotating concentrated circular vortices. Thus, at $t=12$ in the present simulation, all the streamwise vorticity in the braid appears to be concentrated into three pairs of counter-rotating streamwise vortices folding alternatively around the upstream and downstream primary structures, each pair lodging itself within the troughs of the vortex ring (cf. Fig. 2). The streamwise vortices are kept inwards close to the jet axis by the entrainment of the primary vortex rings. But the influence of the rings is gradually counterbalanced by the increasing self-induction of the intensified vortex pairs which tends to expel them outwards. This increasing self-induction may be related to the exponential growth regime of the $u_\varphi(\mathrm{AP})$ curve beyond $t=5$ on Fig. 1. In this connection, one can observe a similar intermediate exponential increase in the NN and WN cases as well, with identical slopes, suggesting that the same mechanism is also present in these two simulations. At $t=14$, as shown in Fig. 1, the azimuthal velocity $u_\varphi(\mathrm{AP})$ reaches the same order of magnitude as $u_r(\mathrm{AP})$: the streamwise structures have become coherent and strong enough, relative to the primary rings, to "free themselves" from the rings influence. Strong positive radial velocity is found all along the jet axis corresponding to the expulsion into secondary planar jets of the fluid located in the vicinity of the streamwise vortex pairs. The strength of this phenomenon can be measured by comparing the u_r curves of the AP and NN cases after $t=14$ in Fig. 1. If the real part of the phase velocity is used to convert time into streamwise distance, this production of side jets should take place, in spatially developing jets, at a streamwise location of about $x/R=6$, in good agreement with experiments.[1,16] Figure 6, which is adapted from a cartoon by Monkewitz and Pfizenmaier,[5] summarizes the configuration of the different vortical structures involved in the side-jet generation process, as synthesized from Figs. 2 and 3: the side jets are induced by pairs of counter-rotating streamwise vortices (hatched structures in Fig. 6) that connect two consecutive distorted vortex rings (white structures). For clarity, only one pair of streamwise vortices is represented. In contrast with the suggestion of Monkewitz and Pfizenmaier, the side jets are located within the advancing troughs of the distorted rings and not around their receding lobes.

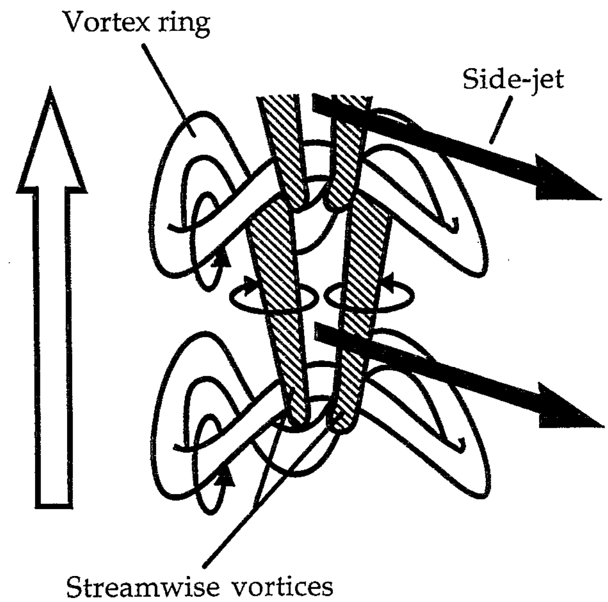

FIG. 6. Vortical structures involved in the side-jet generation process. Only a single streamwise pair is represented (hatched structures) while two consecutive vortex rings are sketched (white structures). The radial ejection of fluid is symbolized by the two black arrows emerging from the streamwise pair.

IV. CONCLUSIONS

The very good agreement found with theory and experiment leads us to conclude that temporally evolving simulations of corrugated jet flows subjected to initial streamwise perturbations reproduce the essential features of side-jet generation. A qualitative description of the side-jet production mechanism has been proposed. Three-dimensional visualizations of both the vorticity and velocity fields have shown the spreading of the jet through secondary planar jets as observed experimentally.[1] These side jets come from velocity induction by pairs of counter-rotating streamwise vortices located in the braid region connecting two consecutive primary vortex rings, in a configuration that slightly differs from previous propositions.[1,5] Though the mechanisms at the origin of the streamwise vorticity giving birth to these longitudinal vortices are still not clearly understood in the "natural," purely circular jet case, a complete scenario for the production of such streamwise vorticity both in the braid and ring regions in the corrugated jet case has been proposed, which is consistent with present numerical simulations.

ACKNOWLEDGMENTS

We wish to thank A. Vincent and M. Meneguzzi for making available to us their numerical code. One of us (P.H.) would like to thank M. Abid and M. E. Brachet for having adapted his two-dimensional eigenvalue code to the axisymmetric case. Thanks are extended to J. P. Brancher for several stimulating discussions about vortex dynamics. Financial support of this work by the Direction des Recherches, Etudes et Techniques (D.R.E.T.) under Grant Nos. 90-040 and 92-1543 is gratefully acknowledged. All

computations were performed on the Cray-2 of the Centre de Calcul Vectoriel pour la Recherche (C.C.V.R.).

[1] P. A. Monkewitz, B. Lehmann, B. Barsikow, and D. W. Bechert, "The spreading of self-excited hot jets by side jets," Phys. Fluids A **1**, 446 (1989).

[2] P. A. Monkewitz, D. W. Bechert, B. Barsikow, and B. Lehmann, "Self-excited oscillations and mixing in a heated round jet," J. Fluid Mech. **213**, 611 (1990).

[3] K. R. Sreenivasan, S. Raghu, and D. Kyle, "Absolute instability in variable density round jets," Exp. Fluids **7**, 309 (1989).

[4] J. C. Lasheras, A. Lecuona, and P. Rodriguez, "Three-dimensional structure of the vorticity field in the near region of laminar co-flowing forced jets," in *The Global Geometry of Turbulence*, edited by J. Jimenez (Plenum, New York, 1991).

[5] P. A. Monkewitz and E. Pfizenmaier, "Mixing by side jets in strongly forced and self-excited round jets," Phys. Fluids A **3**, 1356 (1991).

[6] S. E. Widnall, D. B. Bliss, and C.-Y. Tsai, "The instability of short waves on a vortex ring," J. Fluid Mech. **66**, 35 (1974).

[7] J. E. Martin and E. Meiburg, "Numerical investigation of three-dimensionally evolving jets subject to axisymmetric and azimuthal perturbations," J. Fluid Mech. **230**, 271 (1991).

[8] D. Liepmann and M. Gharib, "The role of streamwise vorticity in the near-field entrainment of round jets," J. Fluid Mech. **245**, 643 (1992).

[9] L. P. Bernal and A. Roshko, "Streamwise vortex structures in plane mixing layers," J. Fluid Mech. **170**, 499 (1986).

[10] R. W. Metcalfe, S. A. Orszag, M. E. Brachet, S. Menon, and J. J. Riley, "Secondary instability of a temporally growing mixing layer," J. Fluid Mech. **184**, 207 (1987).

[11] A. Vincent and M. Meneguzzi, "The spatial structure and statistical properties of homogeneous turbulence," J. Fluid Mech. **225**, 1 (1991).

[12] C. Canuto, M. Y. Hussaini, A. Quarteroni, and T. A. Zang, *Spectral Methods in Fluid Dynamics* (Springer-Verlag, Berlin, 1988).

[13] A. Michalke, "Survey on jet instability theory," Prog. Aerosp. Sci. **21**, 159 (1984).

[14] R. T. Pierrehumbert and S. E. Widnall, "The two- and three-dimensional instabilities of a spatially periodic shear layer," J. Fluid Mech. **114**, 59 (1982).

[15] C. M. Ho and P. Huerre, "Perturbed free shear layers," Annu. Rev. Fluid Mech. **16**, 365 (1984).

[16] S. Raghu, B. Lehmann, and P. A. Monkewitz, "On the mechanism of side-jet generation in periodically excited axisymmetric jets," in *Advances in Turbulence 3*, edited by A. V. Johansson and P. H. Alfredsson (Springer-Verlag, Berlin, 1991).

[17] C. H. Liu, J. Tavantzis, and L. Ting, "Numerical studies of motion and decay of vortex filaments," AIAA J. **24**, 1290 (1986).

[18] S. J. Lin and G. M. Corcos, "The mixing layer: Deterministic models of a turbulent flow. Part 3. The effect of plain strain on the dynamics of streamwise vortices," J. Fluid Mech. **141**, 139 (1984).

[19] J. C. Neu, "The dynamics of stretched vortices," J. Fluid Mech. **143**, 253 (1984).